ChemComm

COMMUNICATION

View Article Online
View Journal

Cite this: DOI: 10.1039/d5cc03565a

Received 24th June 2025,
Accepted 31st July 2025

DOI: 10.1039/d5cc03565a

rsc.li/chemcomm

Fluorine doping of biomass-derived hard carbon for boosted sodium-ion storage

Kongqing Yu,[ab] Tiantian Wei,[ab] Xin Tao,*[ab] Ruilin Zhu,[ab] Jingjing Xie,[ab] Jun Li,*[ab] Huile Jin,*[ab] Shun Wang[ab] and Jichang Wang*[c]

Mainstream hard carbon anode materials in sodium-ion batteries are frequently hindered by issues such as low kinetics for sodium-ion storage. In this work, we present a novel approach to overcome these key limitations by fluorine doping of wheat straw-derived hard carbon, which gives rise to a higher defect density, larger interlayer spacing and faster sodium-ion storage kinetics, when compared to the undoped hard carbon. As a result, the fluorine-doped hard carbon (HCF) exhibits an enhanced rate performance, higher specific capacity and optimized balance between slope and plateau capacity ratios, achieving a reversible capacity of 295 mAh g^{-1} at 1.0 A g^{-1}. This study demonstrates that the intrinsic properties of hard carbon can be efficiently modified through heteroatom doping, offering a promising pathway for the development of high-performance anodes in sodium-ion batteries.

Sodium-ion batteries (SIBs) have emerged as a promising alternative to lithium-ion batteries due to their abundant resources, cost-effectiveness, and better safety profile. Among the various anode materials for SIBs, hard carbon stands out for its wide availability, low cost, and long cycling stability. Despite these merits, hard carbon anodes face significant challenges such as, notably, poor rate performance and low specific capacity, which continue to hinder their application.[1] These issues necessitate further exploration and optimization to unlock the full capabilities of hard carbon in SIBs.

Hard carbon is predominantly derived from biomass precursors, with lesser contributions from synthetic polymers, resins, and coal. Biomass-derived hard carbon features a porous structure with a large surface area, which efficiently enhances sodium-ion storage and transportation. This type of structure provides additional active sites, thereby improving both capacity and rate performance, positioning biomass-derived hard carbon as a promising anode material.[2] For instance, Chou *et al.* synthesized hard carbon anodes by calcining lotus root, while Ma *et al.* used oak leaf biowaste.[3,4] However, both the microstructure and the chemical composition of hard carbon can vary greatly, depending on the precursor, resulting in differing sodium storage mechanisms and a lack of consensus regarding the precise nature of sodium-ion storage.

Various strategies have been explored to improve the physicochemical properties of hard carbon, including microstructure optimization, surface modification, heteroatom doping, composite engineering, and pre-treatment/pre-sodiation techniques.[5] Among these, heteroatom doping has been considered as one of the most effective strategies to enhance the electrochemical performance in SIBs. It modifies the electronic structure, pore distribution, and interfacial chemistry, significantly improving sodium-ion storage capacity, rate capability, and cycling stability.[6] However, heteroatom-doped hard carbon materials still face several critical challenges, such as uneven dopant distribution leading to inconsistent electrochemical properties, structural instability caused by excessive defect sites during long-term cycling, and insufficient understanding of the doping mechanisms at the atomic scale.

In this work, wheat straw-derived hard carbon (HC) was fluorinated *via* a non-contact flow-through method,[7] where pyrolyzed polytetrafluoroethylene (PTFE) served as the upstream fluorine source and the biomass-derived hard carbon was placed downstream for the *ex situ* gas-phase fluorination (Fig. 1a). Wheat straw was selected as a sustainable and abundant biomass precursor, while fluorine—the most electronegative element—was introduced to precisely modulate the local electronic environment of carbon, thereby enhancing Na^+ adsorption and interfacial stability. The *ex situ* fluorine doping enlarges interlayer spacing *via* the formation of C–F bonds and provides new defects and mesopores through gas corrosion, making the fluorine-doped hard carbon (HCF) more suitable for the embedding and detachment of sodium-ions.[8] Additionally, the material demonstrated excellent rate performance and cycling stability, maintaining a capacity of about 295 mAh g^{-1} at 1.0 A g^{-1} with a capacity decay rate of only

[a] Key Laboratory of Leather of Zhejiang Province, Institute of New Materials and Industrial Technologies, Wenzhou University, Wenzhou, Zhejiang, P. R. China. E-mail: hansoli@126.com, huilejin@wzu.edu.cn, taox5802311013@163.com
[b] Zhejiang Engineering Research Center for Electrochemical Energy Materials and Devices, Institute of New Materials and Industrial Technologies, Wenzhou University, Wenzhou, Zhejiang 325035, China
[c] Department of Chemistry and Biochemistry, University of Windsor, Windsor, Ontario, N9B 3P4, Canada. E-mail: jwang@uwindsor.ca

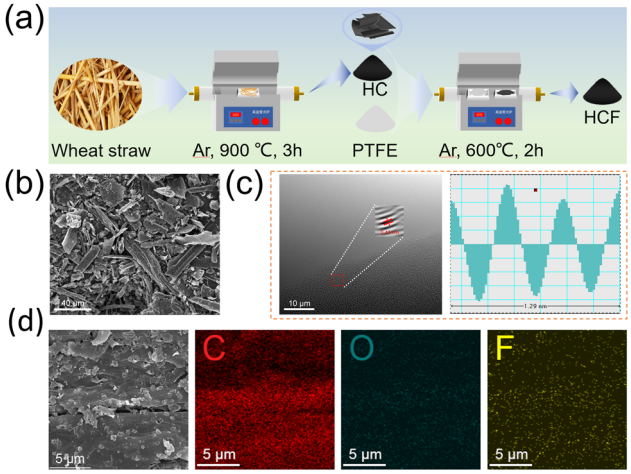

Fig. 1 (a) A schematic diagram depicting the synthesis process of the HCF. (b) SEM images of the HCF-900. (c) HRTEM images of the HCF. (d) corresponding SEM images and element mapping of C, O, F of HCF.

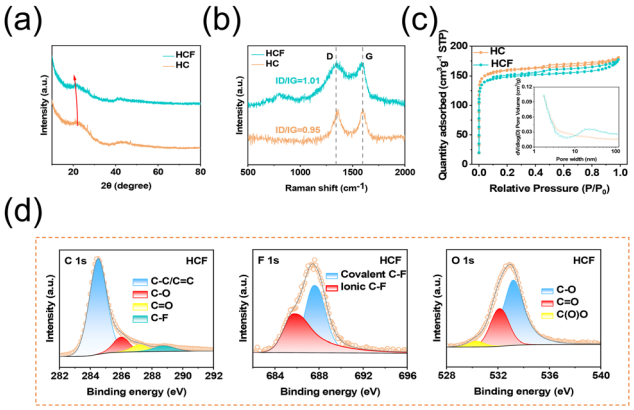

Fig. 2 Structural characterization: (a) XRD patterns of the HCF and HC. (b) Raman spectra of the HCF and HC. (c) N_2 adsorption–desorption isotherm of the HCF and HC and corresponding pore size distribution of the HCF and HC. (d) C 1s and F 1s and O 1s spectra for the HCF.

0.046 mAh g^{-1} per cycle after 1000 cycles. These results highlight the superior electrochemical performance of fluorine-doped biomass porous hard carbon in sodium-ion batteries, with excellent rate capability and capacity retention.

The morphology and structure of the HCF and undoped biomass porous HC were observed using scanning electron microscopy (SEM). As shown in Fig. 1b and Fig. S2, both samples exhibit a lamellar structure, suggesting that fluorine doping does not significantly affect the morphology. The microstructures of HCF and HC were further analyzed using high-resolution transmission electron microscopy (HR-TEM). As shown in Fig. 1c and Fig. S3, the graphitized regions in both samples display short-range order and long-range disorder, forming stacks of 2 to 5 layers. These disordered graphitic layers create a 'house of cards' structure with nanopores, typical of hard carbon.[9] The carbon interlayer spacing for HCF and HC is 0.43 nm and 0.41 nm, respectively, indicating that fluorine doping enlarges the interlayer spacing of HCF, likely through the formation of C–F bonds inside the carbon interlayer, which helps accommodate volume expansion.[10] Energy dispersive X-ray spectroscopy (EDS) analysis in Fig. 1d demonstrates that fluorine atoms are uniformly distributed, confirming the success of the non-contact flow-through *ex situ* doping method.

To investigate the crystal structure of the fluorine-doped hard carbon, X-ray diffraction (XRD) was performed on the HCF and HC. As shown in Fig. 2a, both materials exhibit broad diffraction peaks near 23° and 44°, corresponding to the (002) and (101) planes in the carbon structure.[11] These broad peaks reveal poor crystallinity due to the high structural disorder of hard carbon, with the reduced intensity of the HCF peaks suggesting a higher degree of disorder. Additionally, the (002) peak of the HCF shifts to a lower angle, indicating a larger interlayer spacing compared to the HC.[12] Bragg's equation calculations (eqn (1)) reveal interlayer spacing of 0.41 nm for the HC and 0.43 nm for the HCF, demonstrating that fluorine doping effectively enlarges the interlayer distance, which is consistent with TEM observations.

$$n\lambda = 2d\sin\theta \quad (1)$$

Raman spectroscopy was used to analyze the structure and defects of both materials. As shown in Fig. 2b, both the HCF and HC exhibit distinct peaks at 1342 cm^{-1} (D-band) and 1596 cm^{-1} (G-band), corresponding to defects/porosity in the carbon structure and the graphite structure, respectively.[13] The I_D/I_G ratio for the HCF is 1.01, higher than the HC's ratio of 0.95, indicating more structural defects in the HCF. HF and CF_x segments, generated above 500 °C during the pyrolysis of PTFE, would restructure the micro-/nano-architecture due to their corrosivity and reactivity.[14]

To understand how fluorine doping modifies hard carbon's pore structure and surface area, we analyzed its nitrogen adsorption behavior. The reduced nitrogen uptake in the HCF compared to the HC (Fig. 2c) suggests that fluorine doping seals certain open pores, limiting gas accessibility.[15,16] Notably, pore size distribution demonstrates a shift toward larger pores (>10 nm) in the doped material, suggesting that a mesopore structure is constructed *via* fluorine doping, which enhances its sodium storage capability.[17,18]

To further investigate the surface chemistry, X-ray photoelectron spectroscopy (XPS) analysis was conducted. The XPS fine spectra for the HCF are shown in Fig. 2d. The C 1s spectrum for the HCF displayed four peaks at 284.5, 286.0, 287.2, and 288.8 eV, corresponding to the C–C/C═C, C–O, C═O, and C–F bonds, respectively.[19] The F 1s spectrum exhibited distinct peaks in the range of 684–689 eV, which are attributed to the C–F bonds.[20,21] The O 1s spectrum, with peaks observed at 533.2, 532.1, and 530.3 eV, assigned to the formation of C–O, C═O, and C(O)O bonds, which result from the oxidation of oxygen-containing functional groups in the biomass precursor.[21] Fig. S4 presents the fine spectra of HC, where no significant differences are observed between the C 1s and O 1s spectra. The C 1s spectrum, however, lacks the C–F peak at 288.8 eV, and no F 1s signal is detected. This indicates that fluorine doping introduces only fluorine atoms without affecting the other chemical components. The XPS survey

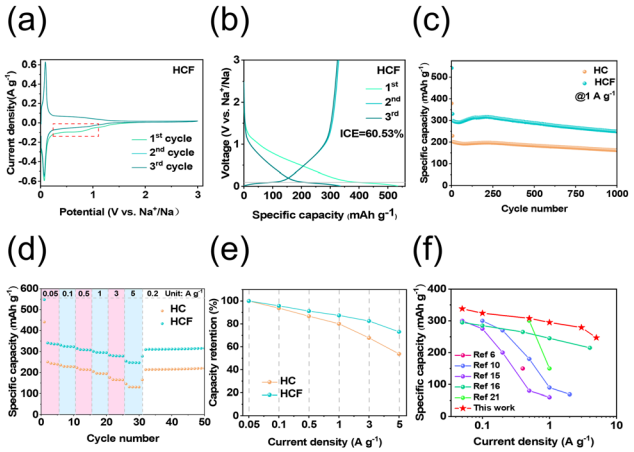

Fig. 3 Electrochemical performance of sodium-ion batteries based on different cathodes. (a) CV curves at a scan rate of 0.1 mV s^{-1} of the HCF electrodes. (b) Galvanostatic charge–discharge profiles of the HCF electrodes. (c) The long-cycle performance of the HCF and HC electrodes at 1 A g^{-1}. (d) Rate performance of the HCF and HC electrodes. (e) Capacity retention at different currents for the HCF and HC electrodes. (f) Comparison of rate performance for the material in this work and reported hard carbon materials.

spectra and elemental ratios of the HC and HCFs with different F/C ratios are shown in Fig. S5 and Table S1.

In this study, sodium metal was used as the counter electrode to form a coin cell for evaluating the electrochemical performance in a half-cell configuration. Fig. 3a and Fig. S6 show the first three cycles of cyclic voltammetry (CV) for the HCF and HC electrodes within a voltage window of 0.01 to 3.0 V at a scan rate of 0.1 mV s^{-1}. A pair of sharp reversible redox peaks, located near 0.075 V, dominate the CVs, indicating the intercalation and pore-filling behavior of sodium-ions in the hard carbon materials.[22] The first-cycle CVs of both the HCF and HC exhibit broad irreversible peaks around 0.3 to 1.5 V, with the HC showing a larger peak area. In contrast, the peak area of the HCF is smaller, suggesting that fluorine doping enhances the reversible capacity and improves the first-cycle coulombic efficiency. In addition to the sharp reversible redox peaks, a pair of broad reversible peaks around 0.50 V is observed for both the HCF and HC, corresponding to sodium adsorption in the hard carbon materials.

Fig. 3b and Fig. S7 show the galvanostatic charge–discharge (GCD) curves measured at 0.1 A g^{-1} for the HCF and HC. The initial coulombic efficiency of the HCF (60.53%) is higher than that of the HC (57.66%), indicating reduced irreversible processes in the HCF. This is consistent with the smaller irreversible peak area in the CV curve. The charge–discharge curves of both materials show similar voltage distributions, divided into a slope region (above 0.1 V) and a plateau region (below 0.1 V), corresponding to the major features in their CV curves. In the current sodium storage model for hard carbon, the slope region corresponds to sodium adsorption at the carbon surface, defects, and functional groups, while the plateau region reflects sodium intercalation into graphitized carbon layers and pore filling.[23] The HCF shows higher capacity in both the slope and plateau regions compared to the HC. As discussed above, fluorine doping enhances defects and functional groups, therefore facilitating sodium-ion adsorption. The plateau region corresponds to intercalation and pore filling, where fluorine doping increases the spacing of graphitized carbon layers and improves the closed pore structure, thus extending the plateau region of the HCF.[24] Fig. S8 shows the contribution of the slope and plateau regions to the reversible capacity, with most of the capacity in both materials coming from the slope region.

Fig. 3c shows the specific capacities and coulombic efficiencies of the HCF and HC over the first 1000 charge/discharge cycles at 1 A g^{-1}. After 1000 cycles, the HCF achieved a reversible capacity of 250 mAh g^{-1}, significantly higher than the 160 mAh g^{-1} of the HC. Furthermore, the coulombic efficiency remained above 99% in subsequent cycles, indicating excellent cycling stability and reversibility. The improved first-cycle coulombic efficiency of the F-doped HC is attributed to fluorine passivation and decreased surface area. Post-cycling SEM (Fig. S9) and XPS (Fig. S10) analyses confirm that the HCF electrode retains structural integrity and stable C–F bonds, indicating robust mechanical and chemical stability.

Fig. 3d shows the rate performance of the HCF and HC at current densities ranging from 0.05 to 5 A g^{-1}. The specific capacities of the HCF at 0.05, 0.1, 0.5, 1.0, 3.0, and 5.0 A g^{-1} are 338, 324, 308, 295, 279, and 247 mAh g^{-1}, respectively, outperforming the HC at all current densities. This enhanced performance is attributed to the increased defects, expanded interlayer spacing, and improved pore structure from fluorine doping, which facilitates the insertion and extraction of sodium-ions, resulting in better kinetic properties.[25] As shown in Fig. 3e, the capacity retention of the HCF is 73.8% at 5.0 A g^{-1}, significantly higher than the HC's 53.78%, demonstrating that fluorine doping helps mitigate capacity loss at high currents and supports fast charging and discharging. In addition, the rate performance of the HCF designed in this work is superior to that of other hard carbon materials and has the potential for fast charging and discharging (Fig. 3f).[6,10,15,16,21] A detailed performance comparison between different elemental doping strategies is provided in the SI (Table S2).

To further confirm that fluorine doping increased the spacing of graphitized carbon layers and modulated the pore structure, thereby enhancing rate performance and specific capacity, cell kinetic tests were performed. CV tests for the HCF and HC were conducted at scan rates ranging from 0.2 to 1.0 mV s^{-1}, as shown in Fig. 4a and Fig. S11. The *b*-values, calculated from the linear relationship between I_p and $V^{0.5}$ (eqn (2)), reveal that the HCF has lower slopes than the HC, as shown in Fig. 4b. This suggests that fluorine doping in the HCF facilitates Na^+ diffusion. To investigate the energy storage mechanism, the capacitance contribution to the total capacity was calculated. As shown in Fig. 4c, the capacitance contribution of the HCF ranges from 81.8% to 91.2% at scan rates of 0.2 to 1.0 mV s^{-1}, indicating that capacitive behavior predominates. In comparison, Fig. S12 shows that the HC has a lower capacitance contribution, indicating that fluorine doping enhances the capacitive behavior and kinetic properties of the HCF.

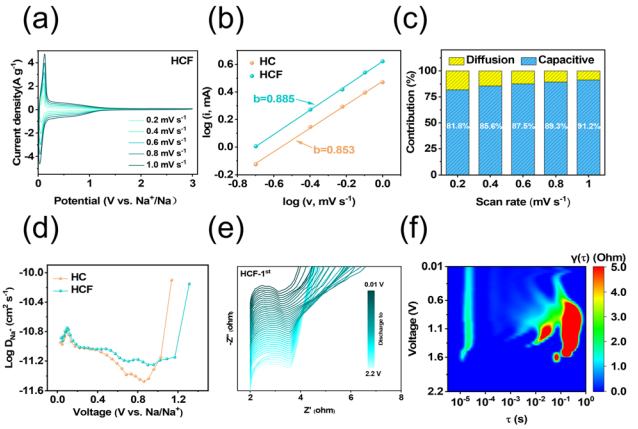

Fig. 4 Battery performance analysis. (a) CV curves of the HCF electrodes at different scan rates of 0.2–1.0 mV s^{-1}. (b) The linear fit relationship between the peak current at 0.075 V and the square root of the scan rate. (c) The capacitive contribution ratio of the HCF electrodes during the capacitance process at different scan rates. (d) Estimated sodium-ion diffusion coefficients from the GITT potential profiles of the HCF and HC electrodes. (e) *In situ* EIS curves of the HCF electrodes at the discharging stage from 2.2 V to 0.01 V. (f) *In situ* distribution of relaxation times of the HCF electrodes at the discharging stage from 2.2 V to 0.01 V.

$$I = av^b \quad (2)$$

$$D_{Zn} = \frac{4}{\pi\tau}\left(\frac{m_B V_M}{M_B A}\right)^2 \left(\frac{\Delta E_s}{\Delta E_\tau}\right)^2 \quad (3)$$

To further investigate the electrochemical kinetics of the HCF and HC, we employed the galvanostatic intermittent titration technique (GITT). The sodium-ion diffusion coefficients (D_{Na^+}) calculated using Fick's second law (eqn (3)) are shown in Fig. 4d, where the HCF exhibits a higher diffusion coefficient than the HC throughout the cycle, suggesting faster sodium-ion diffusion in the HCF. This is likely due to the increased defects and expanded graphitic interlayer spacing from fluorine doping.

In situ electrochemical impedance spectroscopy (EIS) was then used to examine the ion transport properties. Fig. 4e and Fig. S13 show the first discharge cycle EIS for the HCF and HC. The HCF has a lower charge transfer resistance (R_{ct}) than the HC, indicating a faster ion transfer rate. Fig. S14 and S15 display the EIS for the 20th discharge cycle, where both materials show reduced R_{ct} with cycling, but the HCF maintains a lower resistance. The distribution of relaxation time (DRT), derived by deconvoluting the EIS data, reveals additional electrochemical steps not visible in the Nyquist diagram, providing insights into different relaxation times.[26] Fig. 4f and Fig. S13 show the *in situ* DRT for the first discharge cycle of HCF and HC. The high relaxation time region ($\tau \approx 10^{-1}$) represents charge transfer on the electrode surface. For HCF, the peak in the main capacity region (<0.6 V) shifts to a lower relaxation time, suggesting faster sodium storage at the surface and improved insertion kinetics due to fluorine doping. Additionally, the smaller peak intensity of the HCF in the plateau region (<0.1 V) indicates enhanced interfacial kinetics during pore filling. Fig. S14 and S15 show the *in situ* DRT for the 20th discharge cycle, where the HCF exhibits more efficient and balanced charge transfer than the HC, indicating improved kinetics upon fluorine doping.

In summary, this study successfully prepared fluorine-doped biomass carbon with even dopant distribution, a new mesopore structure, enriched defect sites and larger interlayer spacing, which endows the HCF with boosted sodium-ion storage kinetics and superior capacity performance, achieving 295 mAh g^{-1} at 1 A g^{-1} current density for 1000 cycles. The electrochemical performance enhancement due to fluorine doping suggests that fluorine-doped biomass carbon has significant potential for practical application in high-performance sodium-ion batteries.

KQY and TTW contributed equally. We are grateful for the support from the National Natural Science Foundation of China (52472239 and 52272088) and the Natural Sciences and Engineering Research Council of Canada (NSERC, Grant No. 03891).

Conflicts of interest

There are no conflicts to declare.

Data availability

The data supporting this article have been included as part of the SI.

Detailed experimental procedures and synthesis parameters; specifications of characterization instruments; supplementary figures (morphology, structural/chemical analyses, electrochemical performance); supplementary tables (material properties and performance comparisons). See DOI: **https://doi.org/10.1039/d5cc03565a**.

Notes and references

1 F. Wang and Z. Jiang, *et al.*, *eScience*, 2024, **4**, 100181.
2 J. Cui and P. Su, *et al.*, *Adv. Energy Mater.*, 2025, **15**, 2404604.
3 H. Xu and S. Chou, *et al.*, *Nano Energy*, 2025, **137**, 110824.
4 M. Ishaq and Z. Ma, *et al.*, *Adv. Energy Mater.*, 2025, **15**, 2403142.
5 H. Zhang and S. Lin, *et al.*, *Mater. Today*, 2025, **85**, 231–252.
6 C. Yang and W. Zhong, *et al.*, *Carbon Energy*, 2024, **6**, e503.
7 Z. Dai and B. Wang, *et al.*, *RSC Adv.*, 2025, **15**, 9756–9762.
8 A. Rodríguez-Sanz and C. Fuciños, *et al.*, *Int. J. Biol. Macromol.*, 2024, **270**, 132211.
9 N. LeGe and X.-X. He, *et al.*, *Energy Environ. Sci.*, 2023, **16**, 5688–5720.
10 C. Cai and Y. Chen, *et al.*, *Small*, 2022, **18**, 2105303.
11 J. Okabe and Y. Fang, *et al.*, *J. Mater. Chem. A*, 2025, **13**, 13962–13975.
12 X. Lu and J. Zhou, *et al.*, *ACS Appl. Mater. Interfaces*, 2025, **17**, 29708–29719.
13 D. Wang and L. Zhang, *et al.*, *Adv. Funct. Mater.*, 2024, **34**, 2409090.
14 C. Chu and L. L. Ma, *et al.*, *Nat. Commun.*, 2024, **15**, 1654.
15 Y. Wang and Z. Yi, *et al.*, *Adv. Mater.*, 2024, **36**, 2401249.
16 X. Zhang and Y. Cao, *et al.*, *Small*, 2024, **20**, 2311197.
17 Q. Meng and Y. Lu, *et al.*, *ACS Energy Lett.*, 2019, **4**, 2608–2612.
18 J. Lin and Q. Zhou, *et al.*, *Angew. Chem., Int. Ed.*, 2024, **63**, e202409906.
19 Q. Zhang and Q. Shu, *et al.*, *J. Electroanal. Chem.*, 2024, **964**, 118355.
20 Z. Li and L. Kong, *et al.*, *Carbon Energy*, 2023, **5**, e354.
21 B. He and L. Feng, *et al.*, *Chem. Eng. J.*, 2024, **490**, 151636.
22 H. Sun and Q. Zhang, *et al.*, *Energy Storage Mater.*, 2024, **67**, 103269.
23 Nagmani and S. Manna, *et al.*, *Chem. Commun.*, 2024, **60**, 3071–3074.
24 G. Huang and H. Zhang, *et al.*, *Carbon*, 2024, **228**, 119354.
25 S. Xiao and Y. Guo, *et al.*, *Adv. Mater.*, 2025, 2501434.
26 F. Wang and L. Chen, *et al.*, *Energy Environ. Sci.*, 2025, **18**, 4312–4323.

